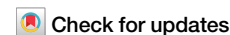




# Interlayer pairing in bilayer nickelates



Thomas A. Maier<sup>1</sup> ✉, Peter Doak<sup>1</sup>, Ling-Fang Lin<sup>2</sup>, Yang Zhang<sup>2,3</sup>, Adriana Moreo<sup>2,3</sup> & Elbio Dagotto<sup>2,3</sup>

The discovery of  $T_c \sim 80$  K superconductivity in pressurized  $\text{La}_3\text{Ni}_2\text{O}_7$  has launched a new platform to study high-temperature superconductivity. Using non-perturbative dynamic cluster approximation quantum Monte Carlo calculations, we characterize the magnetic and superconducting pairing behavior of a realistic bilayer two-orbital Hubbard-Hund model of this system that describes the relevant Ni  $e_g$  states with physically relevant interaction strengths. We find a leading  $s^+$  superconducting instability in this model at a temperature  $T \sim 100$  K close to the experimentally observed  $T_c$ . Analyzing the orbital and spatial structure of the effective pairing interaction giving rise to this state reveals that the interaction predominantly acts between local interlayer pairs of the  $d_{3z^2-r^2}$  orbital. By correlating the strength of the interaction with that of the magnetic spin fluctuations we show that it is driven by strong interlayer spin-fluctuations arising from the  $d_{3z^2-r^2}$  orbital. These results provide first-time non-perturbative evidence supporting the picture that a simple single-orbital bilayer Hubbard model for the Ni  $d_{3z^2-r^2}$  orbital provides an excellent low-energy effective description of the superconducting behavior of  $\text{La}_3\text{Ni}_2\text{O}_7$ .

Superconductivity in pressurized  $\text{La}_3\text{Ni}_2\text{O}_7$ <sup>1,2</sup> has been widely addressed in bilayer two-orbital Hubbard models that account for the  $e_g$  manifold ( $d_{x^2-y^2}$  and  $d_{3z^2-r^2}$  orbitals) of the Ni- $d$  states near the Fermi level in these systems<sup>3–10</sup>. Due to the complexity of the electronic structure, most of these studies have used perturbative, either weak-coupling<sup>4–9,11–14</sup> or strong-coupling<sup>10,15–17</sup> approaches. Depending on details in the model parameters<sup>12</sup> and the type of the approximation, these studies have found  $s^+$ ,  $d_{x^2-y^2}$ , and  $d_{xy}$ -wave superconducting states.

Optical studies, however, show evidence that  $\text{La}_3\text{Ni}_2\text{O}_7$  is characterized by moderately strong electronic correlations<sup>18,19</sup> in the intermediate coupling regime. Consistent with this, recent density functional theory and constrained random-phase approximation (RPA) calculations indeed find that the Hubbard  $U$  interaction on the Ni  $e_g$  orbitals is approximately of the same size as the electronic bandwidth<sup>20</sup>. This raises the question of whether perturbative weak- or strong-coupling approaches can accurately characterize the nature of pairing in these systems, and underscores the need for non-perturbative methods to address this question. While numerical methods such as density matrix renormalization group and tensor networks<sup>21–25</sup>, auxiliary-field Monte Carlo<sup>26</sup>, and cluster dynamical mean-field theory (CDMFT)<sup>27,28</sup> have been used to provide a non-perturbative picture, they are typically based on reduced effective t-J models, simplified interactions, or quasi-one dimensional lattice geometries.

Here, by using state-of-the-art dynamical cluster approximation (DCA) quantum Monte Carlo<sup>29</sup> calculations for a realistic bilayer two-orbital model on a two-dimensional lattice<sup>6</sup> with physically relevant interaction parameters, we examine what this model tells us about the pairing mechanism in the bilayer  $\text{La}_3\text{Ni}_2\text{O}_7$  compound. We find a leading  $s^+$  superconducting instability in this model at a temperature  $T \sim 100$  K close to the experimentally observed

$T_c \sim 80$  K. By analyzing the spatial and orbital structure of the effective pairing interaction, we show that this instability arises from interlayer electron pairing on neighboring sites in the top and bottom layers, primarily in the  $d_{3z^2-r^2}$  orbital. We then analyze the spin correlations in the model and correlate their strength with that of the  $s^+$  pairing interaction to demonstrate that the pairing is primarily driven by interlayer spin fluctuations arising from the  $d_{3z^2-r^2}$  orbital. Our results provide first-time nonperturbative evidence supporting the picture<sup>7</sup> that a single-orbital bilayer Hubbard model<sup>30</sup> for the  $d_{3z^2-r^2}$  orbital provides an appropriate low-energy effective description of the pairing behavior of  $\text{La}_3\text{Ni}_2\text{O}_7$ .

## Results

The model we consider was introduced in ref. 6 and is illustrated in Fig. 1a. Its Hamiltonian is given in the “Methods” section. It includes the two Ni- $3d$  orbitals,  $d_{x^2-y^2}$  and  $d_{3z^2-r^2}$ , that have been found to account for the low-energy electronic structure of the bilayer nickelates. These two orbitals are located on a two-dimensional (2D) square bilayer lattice, and the model includes nearest neighbor hopping, both intra- and inter-layer. It also includes intra-orbital Coulomb  $U$ , inter-orbital Coulomb  $U'$ , and Hund’s rule coupling  $J$  interactions, which we set to  $U = 3$  eV,  $U' = 2$  eV, and  $J = 0.5$  eV (see also “Methods” section).

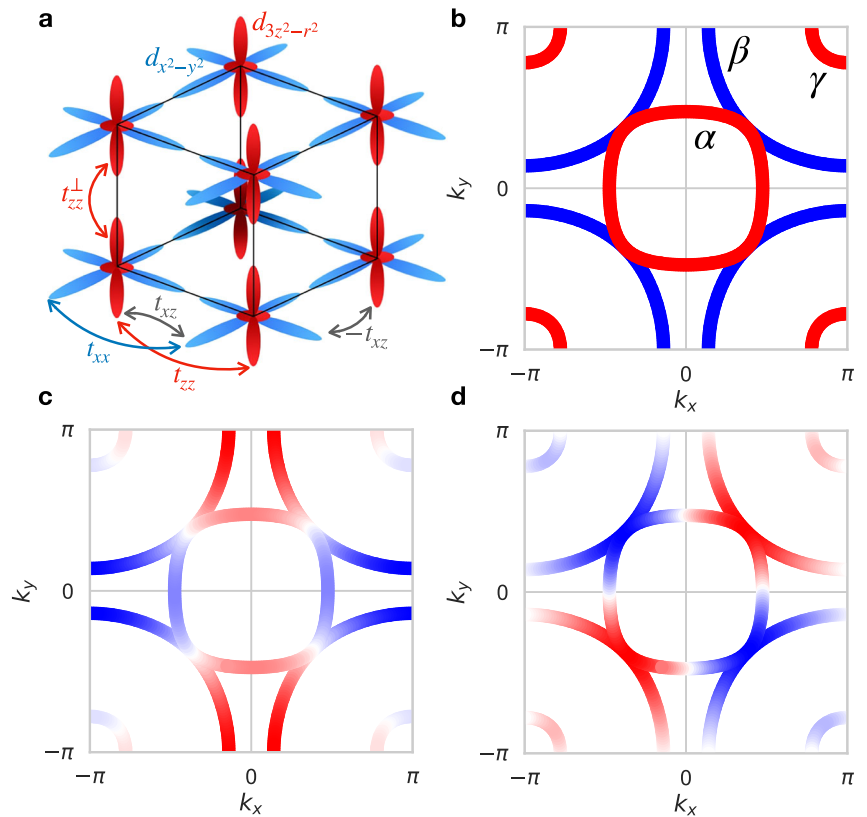
## Pair-field susceptibility

We start by discussing results for the pair-field susceptibility defined as

$$P_\alpha(T) = \int_0^\beta d\tau \langle T_\tau \Delta_\alpha(\tau) \Delta_\alpha^\dagger(0) \rangle \quad (1)$$

<sup>1</sup>Computational Sciences and Engineering Division, Oak Ridge National Laboratory, Oak Ridge, TN, USA. <sup>2</sup>Department of Physics and Astronomy, University of Tennessee, Knoxville, TN, USA. <sup>3</sup>Materials Science and Technology Division, Oak Ridge National Laboratory, Oak Ridge, TN, USA. ✉e-mail: [maiert@ornl.gov](mailto:maiert@ornl.gov)

**Fig. 1 | Illustration of the bilayer two-orbital model and its leading pairing states.** The two orbitals,  $d_{x^2-y^2}$  (blue) and  $d_{3z^2-r^2}$  (red), with nearest neighbor hopping parameters  $t_{xx} = -0.515$ ,  $t_{zz} = -0.110$ ,  $t_{xz} = 0.243$ , and  $t_{zz}^\perp = 0.666$  taken from ref. 6 for 25 GPa pressure are shown in panel (a). The non-interacting Fermi surface consists of  $\alpha$ ,  $\beta$ , and  $\gamma$  sheets as illustrated in (b). The superconducting order parameter form factors listed in Table 1 for  $s^\pm$  (b),  $d_{x^2-y^2}$  (c), and  $d_{xy}$  (d) states are illustrated by red (positive) and blue (negative) colors.



with the pair operator

$$\Delta_\alpha^\dagger = \frac{1}{\sqrt{N}} \sum_{\mathbf{k}, \ell \ell'} g_\alpha^{\ell \ell'}(\mathbf{k}) c_{\mathbf{k} \ell \uparrow}^\dagger c_{-\mathbf{k} \ell' \downarrow}^\dagger \quad (2)$$

Here we have used the momentum space Fourier representation with wave-vector  $\mathbf{k} = (k_x, k_y, k_z)$  with  $k_z = 0$  or  $\pi$  representing bonding and antibonding combinations, respectively, of the two layers,  $c_{\mathbf{k} \ell \sigma}^\dagger = 1/\sqrt{N} \sum_i c_{i \ell \sigma}^\dagger e^{i\mathbf{k} \cdot \mathbf{r}_i}$ , and  $g_\alpha^{\ell \ell'}(\mathbf{k})$  is a symmetry form-factor. The singlet form factors we will use are listed in Table 1 and illustrated in Fig. 1b, c, and d. They correspond to local inter-layer  $s^\pm$  pairs and in-plane  $d_{x^2-y^2}$  and  $d_{xy}$  pairs. We only include intra-orbital components in these form factors, which we expect to dominate, and confirm in the next section through an unbiased analysis that the leading states indeed have substantial intra-orbital pairing character and therefore are captured by these susceptibilities.

As seen in Fig. 1b, the  $s^\pm$  state is negative on the  $\beta$  sheet and positive on the  $\alpha$  and  $\gamma$  pockets. This sign change arises from the difference in bonding/antibonding character of the Fermi surface states on the  $\beta$  and  $\gamma$  pockets<sup>6</sup>. Since the  $d_{x^2-y^2}$  and  $d_{xy}$  states are in-plane states, they are in-phase across all the Fermi surface sheets. In all cases, we only consider intra-orbital pairing. We note that the  $N_c = 2$  site cluster calculation can already address the  $s^\pm$  state, since it contains the two sites (one in the top and one in the bottom layer) that are involved in this pair. It may be regarded as the mean-field solution for this state as it can only fit exactly one  $s^\pm$  pair and therefore cannot capture spatial phase fluctuations (although it fully captures temporal fluctuations). Additionally, the  $N_c = 8$  site cluster can also address the  $d_{x^2-y^2}$  pairing state, but not the  $d_{xy}$  state. The  $N_c = 16$  cluster can resolve all the symmetries we consider.

Figure 2 shows the temperature dependence of the pair-field susceptibility  $P_\alpha(T)$  for the different symmetry channels and cluster sizes. Earlier RPA calculations for the same model found a leading  $s^\pm$  superconducting state, with a sub-leading  $d_{x^2-y^2}$  state<sup>6</sup>. Consistent with this, one sees in Fig. 2 that the  $s^\pm$  susceptibility is rising the most rapidly at low

**Table 1 | Singlet order parameter form factors used for the calculation of the pair-field susceptibility in Eq. (1)**

$\alpha$	$g_\alpha^{\ell \ell'}(\mathbf{k})$
$s^\pm$	$\cos k_z \delta_{\ell \ell'}$
$d_{x^2-y^2}$	$(\cos k_x - \cos k_y) \delta_{\ell \ell'}$
$d_{xy}$	$\sin k_x \sin k_y \delta_{\ell \ell'}$

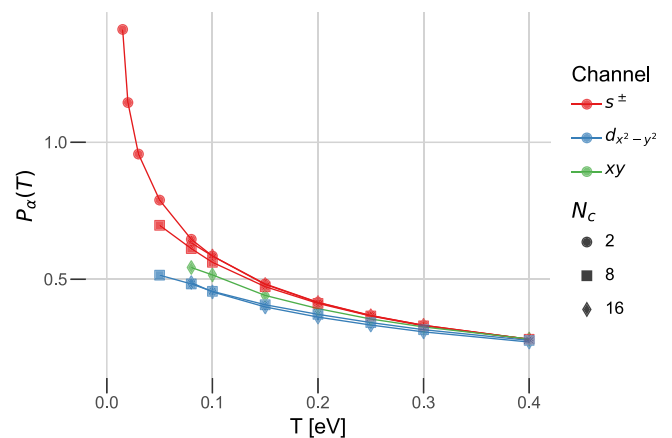
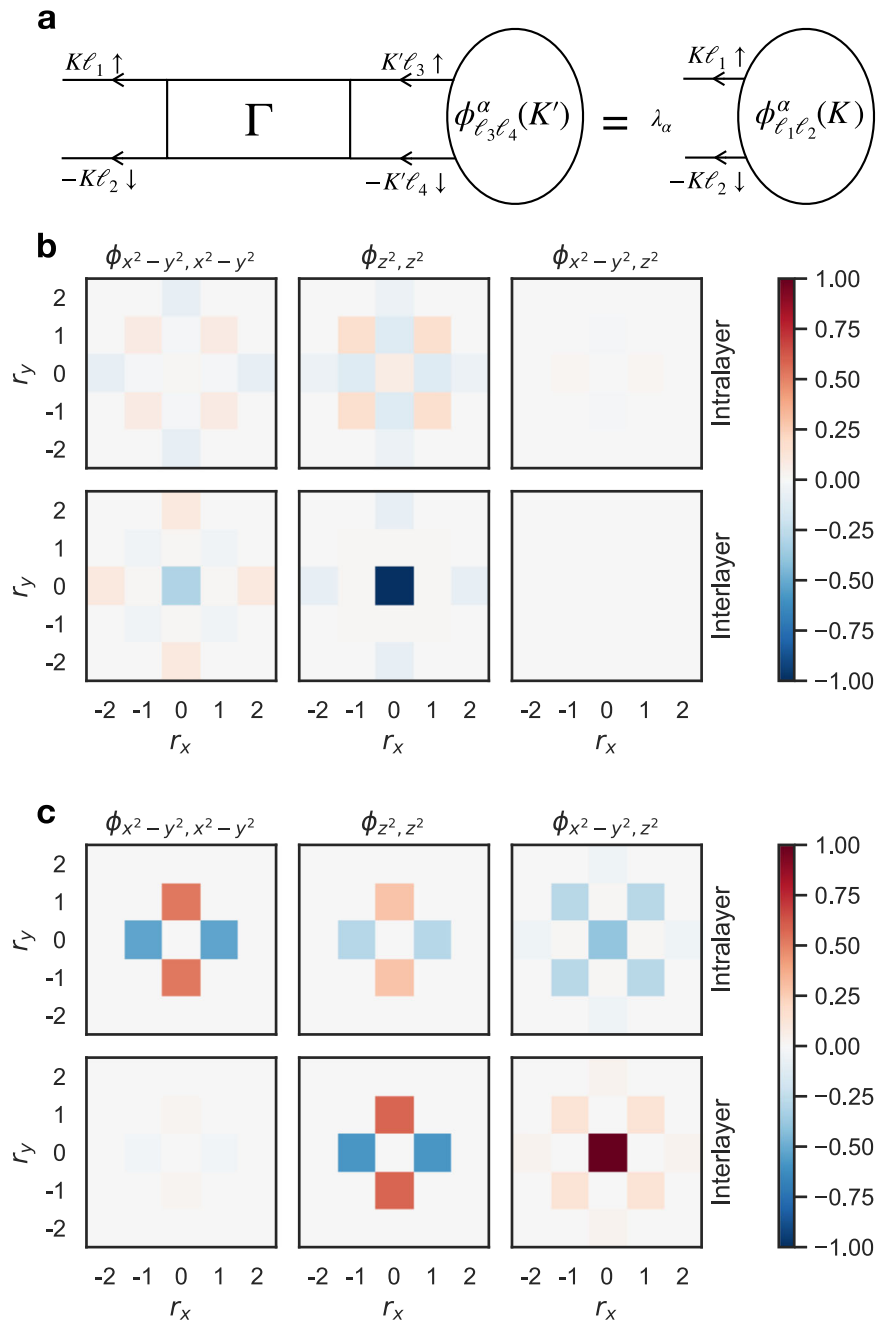


**Fig. 2 | The pair-field susceptibility versus temperature for the two-orbital bilayer 327-LNO model with  $U = 3$  eV,  $U' = 2$  eV, and  $J = 0.5$  eV for different symmetry channels  $\alpha$  and DCA cluster sizes  $N_c$ . The leading  $s^\pm$  symmetry channel has a “mean-field” (see text) superconducting transition near  $T \sim 0.012$  eV  $\sim 140$  K (see Supplemental Material). The QMC statistical errors are small and within the symbol size. A more detailed view of the inverse pair-field susceptibility is shown in Sec. II in the Supplemental Material.**

**Fig. 3 | The orbital and real space structure of the leading pair correlations.** The eigenvalues  $\lambda_\alpha$  and eigenvectors  $\phi_{\ell_1\ell_2}^\alpha(K)$  of the interaction enhanced part of the pair-field susceptibility shown in (a) contain information about the leading pair structures. Panels (b, c) plot the spatial, orbital, and layer structure of the Fourier-transform of  $\phi_{\ell_1\ell_2}^\alpha(K)$  to real space,  $a_{\ell_1\ell_2}^\alpha(\mathbf{r})$ , for the leading  $s^\pm$  ( $\lambda = 0.23$ ) and sub-leading  $d_{x^2-y^2}$  ( $\lambda = 0.1$ ) pair correlations, respectively. Results are for the  $N_c = 16$  site cluster for  $U = 3$  eV,  $U' = 2$  eV,  $J = 0.5$  eV and temperature  $T = 0.08$  eV.



temperatures, followed by the  $d_{xy}$  and  $d_{x^2-y^2}$  susceptibilities. The leading  $s^\pm$  channel shows divergent behavior for the  $N_c = 2$  site cluster indicating an instability near  $T \sim 0.012$  eV  $\sim 140$  K (see also Supplemental Material). This result is consistent with the CDMFT study in ref. 27 for a similar but different model and simplified interaction term with only a  $U$  term on the  $d_{3z^2-r^2}$  orbital. The  $N_c = 8$  results fall below the  $N_c = 2$  results, while the  $N_c = 16$  results are very close to the  $N_c = 2$  results for the temperatures we can access. Lower temperatures are inaccessible for the larger cluster sizes due to the Fermion sign problem. Fluctuations in the cluster size of this sort are expected, since certain clusters, such as  $N_c = 8$ , may overestimate phase fluctuations due to the periodic boundary conditions used on the DCA cluster, and therefore underestimate the pair-field susceptibility. This was previously observed in DCA calculations for the single-orbital Hubbard model<sup>31</sup>. With increasing cluster size, boundary conditions become less important, and one expects this artificial suppression of the pair-field correlations to be reduced. This is indeed what we observe here.

A more detailed analysis of the temperature dependence of the pair-field susceptibilities is included in the Supplemental Material in Sec. II, where we show plots of  $1/P_\alpha$  versus temperature. While the transition temperature is expected to drop in larger clusters due to the inclusion of spatial phase fluctuations, these effects do not appear as pronounced as in the single-orbital Hubbard model<sup>31</sup>, as the the  $N_c = 16$  site results are identical to the  $N_c = 2$  site results down to the lowest temperatures we can access. From this, we conclude that the normal state of this model in the thermodynamic limit has an instability to an  $s^\pm$  superconducting state at a temperature near  $T \sim 0.01$  eV  $\sim 100$  K.

**Orbital and real-space pair structure**

As illustrated in Fig. 3a and detailed in the Supplemental Material, the divergent interaction-driven part of the pair-field susceptibility has the form  $GG\Gamma GG$  with  $G$  the single-particle Green's function and  $\Gamma$  the reducible vertex. The leading eigenvalues  $\lambda_\alpha$  and eigenvectors  $\phi_{\ell_1\ell_2}^\alpha(K)$  of this quantity give information about the frequency and momentum/real-space

structure of the pair correlations that give rise to the enhancement of the pair-field susceptibility. Since we are only interested in spin-singlet, even frequency correlations, we integrate this quantity over frequency as detailed in the Supplemental Material, and show in Fig. 3b and c the real-space, layer, and orbital structure of the two leading eigenvectors,  $\phi_{\ell_1 \ell_2}^\alpha(\mathbf{r}) = 1/N_c \sum_{\mathbf{K}} \phi_{\ell_1 \ell_2}^\alpha(\mathbf{K}) e^{i\mathbf{K}\mathbf{r}}$  for  $\alpha = d_{x^2-y^2}$  and  $d_{xy}$ , respectively. For the leading  $s^\pm$  eigenvector plotted in panel (b) of Fig. 3, the largest contribution arises from the  $d_{3z^2-r^2}$  orbital and has inter-layer and local in-plane character. This corresponds to the  $\cos k_z$  form factor in momentum space. In addition, there is also a much smaller, inter-layer  $\cos k_z$  contribution from the  $d_{x^2-y^2}$  orbital, but only negligible intra-layer nearest- and next-nearest neighbor contributions for both orbitals. Inter-orbital pair correlations do not play a role for this state. The subleading  $d_{x^2-y^2}$  pairing state shown in panel (c) also has a significant inter-layer  $d_{3z^2-r^2}$  contribution, in this case with  $d_{x^2-y^2}$  spatial structure. In contrast to the  $s^\pm$  state in panel b, the  $d_{x^2-y^2}$  orbital contributes strong intra-layer but no inter-layer correlations. Another difference is the presence of strong inter-orbital pair correlations, which have opposite signs for intra- and inter-layer contributions. These contributions necessarily have  $s$ -wave spatial structure, which, together with the overall  $d_{x^2-y^2}$  orbital structure of the inter-orbital pairs, gives the net  $d_{x^2-y^2}$ -wave pair structure.

Notably, we find that the first state with  $d_{xy}$ -wave structure (not shown) has a significantly smaller eigenvalue than the  $s^\pm$  and  $d_{x^2-y^2}$  states shown in Fig. 3. This means that the  $d_{xy}$ -wave pair-field correlations shown in Fig. 2, even though they are larger than the  $d_{x^2-y^2}$ -wave correlations, arise mostly from the leading (zeroth order in the interaction) contribution to  $P_{d_{xy}}$  and are not significantly enhanced by the interactions and therefore not divergent at lower temperatures.

### Magnetic susceptibility

Spin fluctuations have been argued to play an important role in mediating the pairing in unconventional superconductors like the nickelates. It is therefore interesting to study whether their structure is consistent with the observed pairing correlations. The zero frequency magnetic susceptibility is given by

$$\chi(\mathbf{q}) = \sum_{\ell_1 \ell_2} \int_0^\beta d\tau \langle m_{q\ell_1}^-(\tau) m_{q\ell_2}^\dagger(0) \rangle \quad (3)$$

with  $m_{q\ell}^\dagger = 1/\sqrt{N} \sum_{\mathbf{k}} d_{\mathbf{k}+\mathbf{q}\ell\uparrow}^\dagger d_{\mathbf{k}\ell\downarrow}$  and  $\mathbf{q} = (q_x, q_y, q_z)$  with  $q_z = 0$  and  $\pi$  the even and odd layer combinations, respectively. We plot in Fig. 4, the temperature dependence of  $\chi(\mathbf{q})$  calculated on the  $N_c = 16$  cluster and interpolated in  $(q_x, q_y)$ . For all temperatures, the inter-layer antiferromagnetic ( $q_z = \pi$ ) correlations are stronger than the inter-layer ferromagnetic ( $q_z = 0$ ) correlations. As the temperature is lowered, peaks develop for in-plane  $\mathbf{q} = (\pi, 0)$  and symmetry-related points for  $q_z = \pi$ , so that at the lowest temperature, the strongest response is obtained for  $\mathbf{q} = (\pi, 0, \pi)$ . This corresponds to in-plane striped (antiferromagnetic along  $q_x$ , ferromagnetic along  $q_y$ ) and inter-layer antiferromagnetic correlations. These results are consistent with earlier weak coupling RPA calculations for this model in ref. 6,32.

### Pairing interaction

A measure of the strength of the pairing interaction giving rise to the pairing states  $\alpha$  shown in Fig. 3 is

$$V_\alpha(T) = \frac{1}{P_{\phi^\alpha}(T)} - \frac{1}{P_{\phi^\alpha}^0(T)}. \quad (4)$$

As detailed in the Supplemental Material,  $P_{\phi^\alpha}$  is the pair-field susceptibility in Eq. (1) using for the form factor  $g_{\ell\ell'}^\alpha = \phi_{\ell\ell'}^\alpha$ , i.e., the leading eigenvectors shown in Fig. 3, and  $P_{\phi^\alpha}^0$  is the leading (zeroth order) term in the Bethe-

Salpeter expansion of  $P_{\phi^\alpha}$ . A plot of  $V_\alpha(T)$  is shown in Fig. 5a. In Fig. 5b, we have plotted the integrated spin fluctuation spectral weights

$$\begin{aligned} I_v &= \frac{1}{N_c} \sum_{\mathbf{Q}} \int \frac{d\omega}{\pi} \frac{\chi''(\mathbf{Q}, \omega)}{\omega} \cos Q_v \\ &= \frac{1}{N_c} \sum_{\mathbf{Q}} \chi(\mathbf{Q}) \cos Q_v \end{aligned} \quad (5)$$

for the intra- ( $Q_v = Q_x$ ) and inter-layer ( $Q_v = Q_z$ ) near-neighbor spin fluctuations. Here, the sum over  $\mathbf{Q}$  runs over the  $N_c$  cluster momenta. The pairing interaction  $V_\alpha(T)$  increases as the temperature  $T$  is lowered for both pairing channels  $\alpha = s^\pm$  and  $d_{x^2-y^2}$ . Similarly, the near-neighbor inter-layer spin-fluctuation spectral weight  $I_z$  also increases as  $T$  decreases. This increase arises from the increasing difference between the inter-layer antiferromagnetic ( $q_z = \pi$ ) and ferromagnetic ( $q_z = 0$ ) spin correlations shown in Fig. 4 as  $T$  decreases. In contrast, the intra-layer spectral weight  $I_x$  remains small for all the temperatures indicating that intra-layer spin fluctuations do not play an important role. The dashed line for the  $\ell_1, \ell_2 = d_{3z^2-r^2}$  contribution in panel (b) shows that  $I_z$  primarily arises from spin fluctuations in the  $d_{3z^2-r^2}$  orbital. Taken together, we believe that this demonstrates that both pairing states,  $s^\pm$  and  $d_{x^2-y^2}$ , are primarily driven by inter-layer spin fluctuations arising from the  $d_{3z^2-r^2}$  orbital.

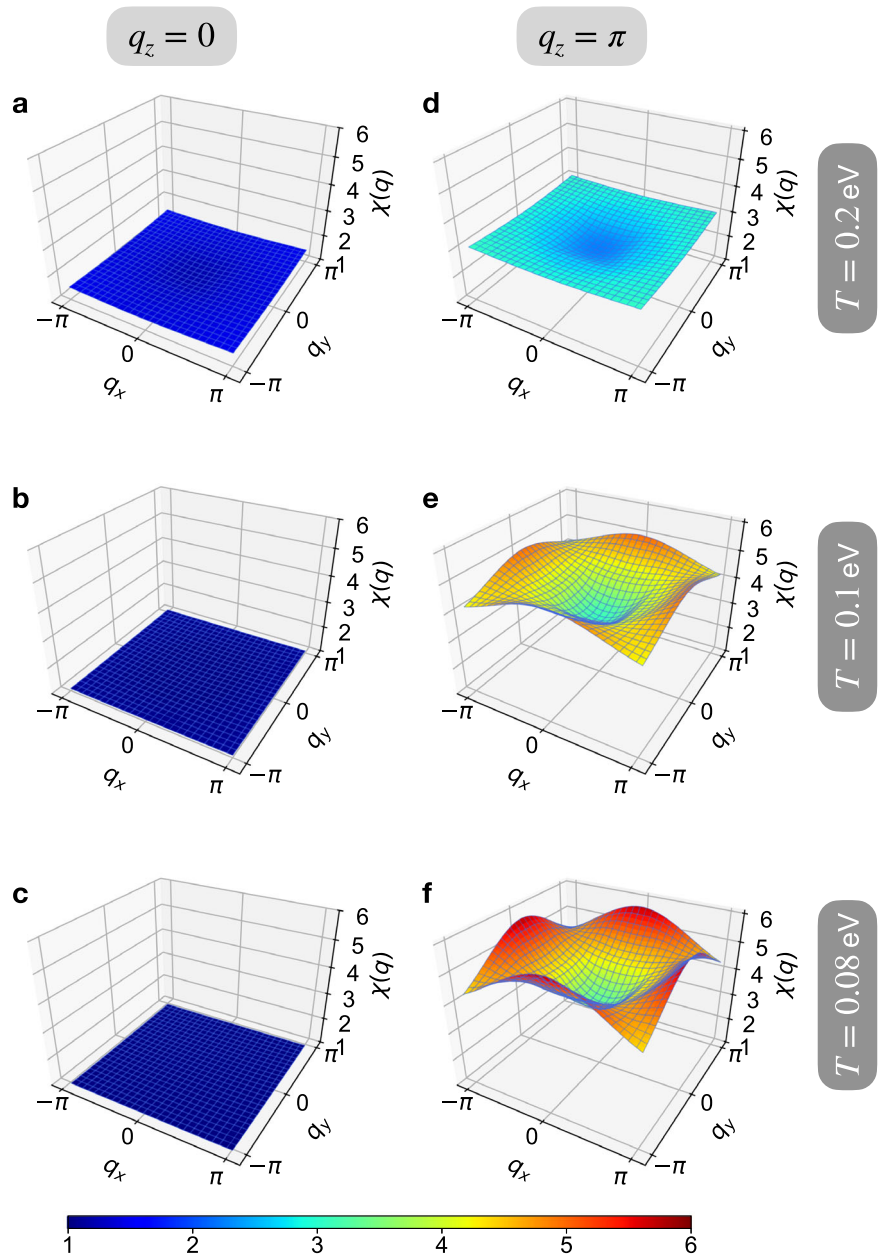
### Discussion

Our nonperturbative analysis of the effective pairing interaction demonstrates that the  $d_{3z^2-r^2}$  orbital is the primary orbital involved in the pairing mechanism, giving rise to the  $s^\pm$  state. From Fig. 3b it is clear that for the leading  $s^\pm$  state, pairing is mostly limited to the  $d_{3z^2-r^2}$  orbital, and Fig. 5 shows that it is the  $d_{3z^2-r^2}$  inter-layer spin fluctuations that give rise to this state. These results support the picture of a simple single-orbital bilayer Hubbard model first discussed by Sakakibara et al. in ref. 7 in the context of weak-coupling perturbative calculations, where the  $d_{3z^2-r^2}$  orbital is the relevant orbital and the  $d_{x^2-y^2}$  orbital plays a secondary role. Previous DCA QMC calculations for such a single-orbital bilayer Hubbard model with interlayer hopping  $t_\perp$  found a similar leading  $s^\pm$  pairing state for parameter regimes where  $t_\perp$  is larger than the in-plane nearest neighbor hopping  $t^{30}$ . The present two-orbital model has similar relative energy scales, where the inter-layer hopping  $t_{zz}^\perp$  for the  $d_{3z^2-r^2}$  orbital is the largest hopping in the model. While there are differences in the momentum structure of the spin fluctuations (in the single-band model the scattering is peaked at an in-plane  $\mathbf{q} = (\pi, \pi)$  wavevector<sup>30</sup> rather than the  $(\pi, 0)$  wavevector found here), the dominant inter-layer nature of the spin fluctuations and their role in driving the  $s^\pm$  pairing state is consistent between the two models.

Our results provide first-time nonperturbative evidence for this picture and strengthen the notion that  $T_c$  in bilayer  $\text{La}_3\text{Ni}_2\text{O}_7$  can be further increased because of its relation to the simple bilayer Hubbard model<sup>7</sup>, for which previous DCA QMC calculations found a significantly enhanced  $T_c^{30}$ . Strategies to achieve such an enhancement by tuning the electronic structure in ways that result in a self-doping of the  $d_{3z^2-r^2}$  orbital were discussed in ref. 7.

To conclude, in this work, we have reported DCA QMC calculations for a realistic bilayer two-orbital Hubbard-Hund model of  $\text{La}_3\text{Ni}_2\text{O}_7$  that allowed us to study the pairing mechanism in this material for physically relevant interaction parameters nonperturbatively. We have shown that this model has an  $s^\pm$  superconducting instability with singlet pairs formed primarily from electrons in the  $d_{3z^2-r^2}$  orbitals on neighboring sites in the top and bottom layers, and that this pair formation is driven by strong inter-layer spin fluctuations arising from the  $d_{3z^2-r^2}$  orbitals. These results provide new evidence for a simple bilayer Hubbard model picture of pairing in these compounds, for which previous calculations have found an enhanced  $T_c$  supporting the possibility that  $T_c$  in  $\text{La}_3\text{Ni}_2\text{O}_7$  can be further increased through electronic structure tuning.

**Fig. 4 | Magnetic correlations in the bilayer two-orbital model.** In-plane ( $q_x, q_y$ ) dependence of the cluster magnetic susceptibility  $\chi(\mathbf{q})$  for  $q_z = 0$  ((a, b, c)) and  $q_z = \pi$  ((d, e, f)) for three different temperatures as indicated on the right. As the temperature is lowered,  $\chi(\mathbf{q})$  develops peaks for  $\mathbf{q} = (\pi, 0, \pi)$  and symmetry-related wavevectors. Results are for  $U = 3$  eV,  $U' = 2$  eV, and  $J = 0.5$  eV.



**Methods**

**Bilayer two-orbital model**

The Hamiltonian of the bilayer two-orbital model we consider

$$H = H_0 + H_{int} \tag{6}$$

consists of a non-interacting tight-binding part  $H_0$  and an interaction term  $H_{int}$ . The non-interacting term is given by

$$H_0 = \sum_{(ij)} \sum_{\ell\ell',\sigma} t_{\ell\ell'}^{ij} (d_{i\ell\sigma}^\dagger d_{j\ell'\sigma} + h.c.) + \epsilon_x \sum_{i\sigma} n_{i\sigma} - \mu \sum_{i\ell\sigma} n_{i\ell\sigma} \tag{7}$$

Here,  $t_{\ell\ell'}^{ij}$  is the hopping amplitude between orbitals  $\ell, \ell' \in \{x \equiv d_{x^2-y^2}, z \equiv d_{3z^2-r^2}\}$  on nearest neighbor sites  $i, j$  in the bilayer lattice,  $d_{i\ell\sigma}$  ( $d_{i\ell\sigma}^\dagger$ ) annihilates (creates) an electron with spin  $\sigma$  on site  $i$  in orbital  $\ell$  and  $n_{i\ell\sigma} = d_{i\ell\sigma}^\dagger d_{i\ell\sigma}$ . The values for  $t_{\ell\ell'}^{ij}$  are given in the caption of Fig. 1 and

correspond to the system under 25 GPa pressure. We note that the largest hopping parameter is the intra-orbital, inter-layer hopping  $t_{zz}^\perp$  between the  $d_{3z^2-r^2}$  orbitals, leading to bonding and antibonding states as discussed in ref. 6. Finally,  $\epsilon_x = 0.506$  eV denotes the crystal field splitting between the  $d_{x^2-y^2}$  and  $d_{3z^2-r^2}$  orbitals. The chemical potential  $\mu$  is adjusted so that the total site filling  $\langle n \rangle = 1.5$ , which corresponds to stoichiometric  $\text{La}_3\text{Ni}_2\text{O}_7$ .

The interaction term is given by

$$H_{int} = U \sum_i n_{i\ell\uparrow} n_{i\ell\downarrow} + \frac{U'}{2} \sum_i \sum_{\ell \neq \ell', \sigma, \sigma'} n_{i\ell\sigma} n_{i\ell'\sigma'} + \frac{U'-J}{2} \sum_i \sum_{\ell \neq \ell', \sigma} n_{i\ell\sigma} n_{i\ell'\sigma} \tag{8}$$

and contains the local intra-orbital and inter-orbital Coulomb repulsions  $U$  and  $U'$ , respectively, as well as the density-density part of the Hund's rule coupling  $J$ . Here, we have neglected the spin-flip part of the Hund's

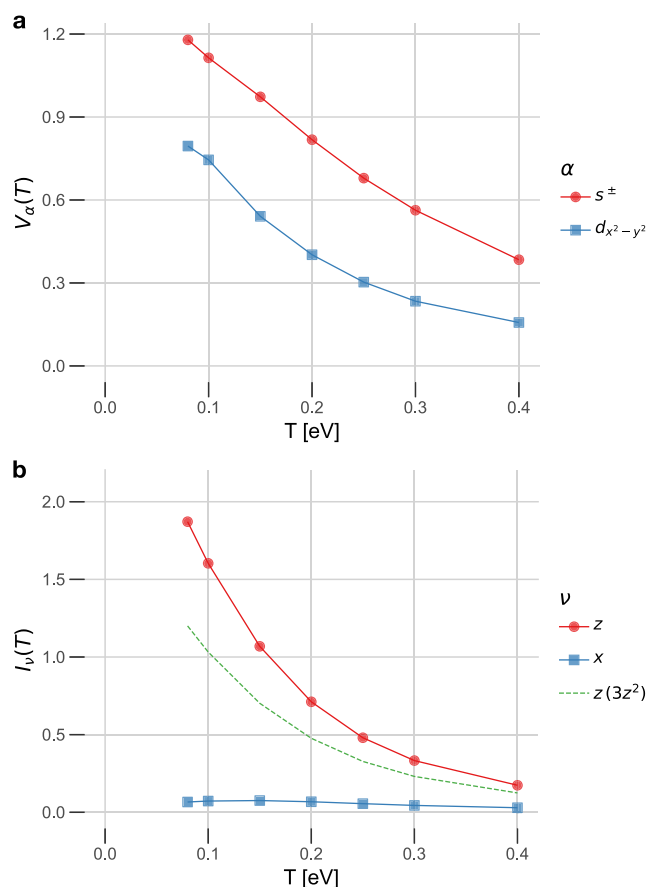


**Fig. 5 | Temperature dependence of the pairing interaction and the spin fluctuations.** The strength of (a) the pairing interaction  $V_\alpha$  for  $\alpha = s^\pm$  and  $d_{x^2-y^2}$  calculated from Eq. (4) and (b) the integrated spin fluctuation spectral weight  $I_\nu$ , Eq. (5), versus temperature. The dashed line in (b) shows the  $d_{3z^2-r^2}$  contribution to the  $\nu = z$  spectral weight. Results are for the  $N_c = 16$  cluster and  $U = 3$  eV,  $U' = 2$  eV, and  $J = 0.5$  eV.

rule coupling as well as the pair-hopping term. These terms are known to cause difficulties in the QMC treatment by significantly exacerbating the Fermion sign problem<sup>33</sup>. These neglected terms have been shown to only mildly affect the phase diagram of a three-orbital Hubbard model<sup>34</sup>. All the results presented in this paper are for  $U = 3$  eV,  $U' = 2$  eV, and  $J = 0.5$  eV. These values are representative of the parameters that have been determined from optical properties<sup>19</sup> and have been used before in other calculations<sup>7</sup>.

### Dynamical cluster quantum Monte Carlo approximation

We calculate the pairing and magnetic properties of this model using a DCA approximation<sup>29,35</sup>, which approximates the thermodynamic limit by a finite-size  $N_c$ -site cluster that is self-consistently embedded in a dynamic mean-field designed to treat the effects of the remaining sites in the lattice. The effective cluster problem is solved with a continuous-time auxiliary field quantum Monte Carlo algorithm<sup>36,37</sup>. The efficient implementation of this DCA QMC algorithm in the DCA++ code<sup>38</sup> allows us to perform sufficiently long sampling to accurately resolve the superconducting properties. We have used a two-site  $(1 \times 1) \times 2$  cluster ( $N_c = 2$ ) with one site in the bottom and one site in the top layer, an 8-site  $(2 \times 2) \times 2$  cluster with four  $(2 \times 2)$  sites per layer ( $N_c = 8$ ), and a 16-site cluster with 8 sites (in a diamond shape) per layer ( $N_c = 16$ ).

### Data availability

The data that support the findings of this study can be obtained at Zenodo at <https://doi.org/10.5281/zenodo.17945044>.

### Code availability

The DCA++ code used in this study is available at <https://github.com/CompFUSE/DCA>.

Received: 9 July 2025; Accepted: 4 January 2026;

Published online: 22 January 2026

### References

1. Sun, H. et al. Signatures of superconductivity near 80 K in a nickelate under high pressure. *Nature* **621**, 493–498 (2023).
2. Hou, J. et al. Emergence of high-temperature superconducting phase in pressurized  $\text{La}_3\text{Ni}_2\text{O}_7$  crystals. *Chin. Phys. Lett.* **40** (2023).
3. Luo, Z., Hu, X., Wang, M., Wú, W. & Yao, D.-X. Bilayer two-orbital model of  $\text{La}_3\text{Ni}_2\text{O}_7$  under pressure. *Phys. Rev. Lett.* **131**, 126001 (2023).
4. Liu, Y.-B., Mei, J.-W., Ye, F., Chen, W.-Q. & Yang, F.  $s^\pm$ -wave pairing and the destructive role of apical-oxygen deficiencies in  $\text{La}_3\text{Ni}_2\text{O}_7$  under pressure. *Phys. Rev. Lett.* **131**, 236002 (2023).
5. Lechermann, F., Gondolf, J., Bötzel, S. & Eremin, I. M. Electronic correlations and superconducting instability in  $\text{La}_3\text{Ni}_2\text{O}_7$  under high pressure. *Phys. Rev. B* **108**, L201121 (2023).
6. Zhang, Y., Lin, L.-F., Moreo, A., Maier, T. A. & Dagotto, E. Structural phase transition,  $s \pm$ -wave pairing, and magnetic stripe order in bilayered superconductor  $\text{La}_3\text{Ni}_2\text{O}_7$  under pressure. *Nat. Comm.* **15**, 2470 (2024).
7. Sakakibara, H., Kitamine, N., Ochi, M. & Kuroki, K. Possible high  $T_c$  superconductivity in  $\text{La}_3\text{Ni}_2\text{O}_7$  under high pressure through manifestation of a nearly half-filled bilayer Hubbard model. *Phys. Rev. Lett.* **132**, 106002 (2024).
8. Gu, Y., Le, C., Yang, Z., Wu, X. & Hu, J. Effective model and pairing tendency in the bilayer Ni-based superconductor  $\text{La}_3\text{Ni}_2\text{O}_7$ . *Phys. Rev. B* **111**, 174506 (2025).
9. Xi, W., Yu, S.-L. & Li, J.-X. Transition from  $s \pm$ -wave to  $dx_2-y_2$ -wave superconductivity driven by interlayer interaction in the bilayer two-orbital model of  $\text{La}_3\text{Ni}_2\text{O}_7$ . *Phys. Rev. B* **111**, 104505 (2025).
10. Yang, Y.-f, Zhang, G.-M. & Zhang, F.-C. Interlayer valence bonds and two-component theory for high- $T_c$  superconductivity of  $\text{La}_3\text{Ni}_2\text{O}_7$  under pressure. *Phys. Rev. B* **108**, L201108 (2023).
11. Bötzel, S., Lechermann, F., Gondolf, J. & Eremin, I. M. Theory of magnetic excitations in the multilayer nickelate superconductor  $\text{La}_3\text{Ni}_2\text{O}_7$ . *Phys. Rev. B* **109**, L180502 (2024).
12. Xia, C., Liu, H., Zhou, S. & Chen, H. Sensitive dependence of pairing symmetry on Ni-eg crystal field splitting in the nickelate superconductor  $\text{La}_3\text{Ni}_2\text{O}_7$ . *Nat. Comm.* **16**, 1054 (2025).
13. Heier, G., Park, K. & Savrasov, S. Y. Competing  $d_{xy}$  and  $s_\pm$  pairing symmetries in superconducting  $\text{La}_3\text{Ni}_2\text{O}_7$ : LDA + FLEX calculations. *Phys. Rev. B* **109**, 104508 (2024).
14. Yang, Q.-G., Wang, D. & Wang, Q.-H. Possible  $s_\pm$ -wave superconductivity in  $\text{La}_3\text{Ni}_2\text{O}_7$ . *Phys. Rev. B* **108**, L140505 (2023).
15. Lu, C., Pan, Z., Yang, F. & Wu, C. Interlayer-coupling-driven high-temperature superconductivity in  $\text{La}_3\text{Ni}_2\text{O}_7$  under pressure. *Phys. Rev. Lett.* **132**, 146002 (2024).
16. Liao, Z. et al. Electron correlations and superconductivity in  $\text{La}_3\text{Ni}_2\text{O}_7$  under pressure tuning. *Phys. Rev. B* **108**, 214522 (2023).
17. Jiang, K., Wang, Z. & Zhang, F.-C. High-temperature superconductivity in  $\text{La}_3\text{Ni}_2\text{O}_7$ . *Chin. Phys. Lett.* **41**, 017402 (2024).
18. Liu, Z. et al. Electronic correlations and partial gap in the bilayer nickelate  $\text{La}_3\text{Ni}_2\text{O}_7$ . *Nat. Comm.* **15**, 7570 (2024).
19. Geisler, B. et al. Optical properties and electronic correlations in  $\text{La}_3\text{Ni}_2\text{O}_7$  bilayer nickelates under high pressure. *npj Quantum Materials* **9**, 89 (2024).
20. Yue, C. et al. Correlated electronic structures and unconventional superconductivity in bilayer nickelate heterostructures. <https://arxiv.org/abs/2501.06875> (2025).
21. Shen, Y., Qin, M. & Zhang, G.-M. Effective bi-layer model Hamiltonian and density-matrix renormalization group study for the high- $T_c$

- superconductivity in La<sub>3</sub>Ni<sub>2</sub>O<sub>7</sub> under high pressure. *Chin. Phys. Lett.* **40**, 127401 (2023).
22. Qu, X.-Z. et al. Bilayer  $t-J-J_{\perp}$  model and magnetically mediated pairing in the pressurized nickelate La<sub>3</sub>Ni<sub>2</sub>O<sub>7</sub>. *Phys. Rev. Lett.* **132**, 036502 (2024).
  23. Schlömer, H., Schollwöck, U., Grusdt, F. & Bohrdt, A. Superconductivity in the pressurized nickelate La<sub>3</sub>Ni<sub>2</sub>O<sub>7</sub> in the vicinity of a BEC-BCS crossover. *Comm. Phys.* **7**, 366 (2024).
  24. Kaneko, T., Sakakibara, H., Ochi, M. & Kuroki, K. Pair correlations in the two-orbital Hubbard ladder: Implications for superconductivity in the bilayer nickelate La<sub>3</sub>Ni<sub>2</sub>O<sub>7</sub>. *Phys. Rev. B* **109**, 045154 (2024).
  25. Kakoi, M., Kaneko, T., Sakakibara, H., Ochi, M. & Kuroki, K. Pair correlations of the hybridized orbitals in a ladder model for the bilayer nickelate La<sub>3</sub>Ni<sub>2</sub>O<sub>7</sub>. *Phys. Rev. B* **109**, L201124 (2024).
  26. Qin, Q. & Yang, Y.  $f$  High- $T_c$  superconductivity by mobilizing local spin singlets and possible route to higher  $T_c$  in pressurized La<sub>3</sub>Ni<sub>2</sub>O<sub>7</sub>. *Phys. Rev. B* **108**, L140504 (2023).
  27. Zheng, Y.-Y. & Wú, W.  $s \pm$   $-$ wave superconductivity in the bilayer two-orbital Hubbard model. *Phys. Rev. B* **111**, 035108 (2025).
  28. Tian, Y.-H., Chen, Y., Wang, J.-M., He, R.-Q. & Lu, Z.-Y. Correlation effects and concomitant two-orbital  $s \pm$   $-$ wave superconductivity in La<sub>3</sub>Ni<sub>2</sub>O<sub>7</sub> under high pressure. *Phys. Rev. B* **109**, 165154 (2024).
  29. Maier, T., Jarrell, M., Pruschke, T. & Hettler, M. Quantum cluster theories. *Rev. Mod. Phys.* **77**, 1027–1080 (2005).
  30. Maier, T. A. & Scalapino, D. J. Pair structure and the pairing interaction in a bilayer Hubbard model for unconventional superconductivity. *Phys. Rev. B* **84**, 3–6 (2011).
  31. Maier, T. A., Jarrell, M., Schulthess, T. C., Kent, P. R. C. & White, J. B. Systematic Study of d-Wave Superconductivity in the 2D Repulsive Hubbard Model. *Phys. Rev. Lett.* **95**, 237001–237001 (2005).
  32. Zhang, Y., Lin, L.-F., Moreo, A. & Dagotto, E. Electronic structure, dimer physics, orbital-selective behavior, and magnetic tendencies in the bilayer nickelate superconductor La<sub>3</sub>Ni<sub>2</sub>O<sub>7</sub> under pressure. *Phys. Rev. B* **108**, L180510 (2023).
  33. Troyer, M. & Wiese, U. Computational complexity and fundamental limitations to fermionic quantum Monte Carlo simulations. *Phys. Rev. Lett.* **94**, 170201–170201 (2005).
  34. Liu, G. et al. Orbital-selective Mott phases of a one-dimensional three-orbital Hubbard model studied using computational techniques. *Phys. Rev. E* **93**, 063313 (2016).
  35. Hettler, M. H., Tahvildar-Zadeh, A. N., Jarrell, M., Pruschke, T. & Krishnamurthy, H. R. Nonlocal dynamical correlations of strongly interacting electron systems. *Phys. Rev. B* **58**, R7475–R7479 (1998).
  36. Gull, E., Millis, A. J., Lichtenstein, A. I., Troyer, M. & Werner, P. Continuous-time Monte Carlo methods for quantum impurity models. *Rev. Mod. Phys.* **83**, 349–404 (2011).
  37. Gull, E. et al. Submatrix updates for the continuous-time auxiliary-field algorithm. *Phys. Rev. B* **83**, 75122–75122 (2011).
  38. Hähner, U. R. et al. DCA++: a software framework to solve correlated electron problems with modern quantum cluster methods. *Comp. Phys. Commun.* **246**, 106709 (2020).

## Acknowledgements

This work was supported by the U.S. Department of Energy, Office of Science, Basic Energy Sciences, Materials Sciences and Engineering Division. An award of computer time was provided by the INCITE program. This research also used resources of the Oak Ridge Leadership Computing Facility, which is a DOE Office of Science User Facility supported under Contract DE-AC05-00OR22725. This manuscript has been authored by UT-Battelle, LLC, under Contract No. DE-AC0500OR22725 with the U.S. Department of Energy. The United States Government retains and the publisher, by accepting the article for publication, acknowledges that the United States Government retains a nonexclusive, paid-up, irrevocable, worldwide license to publish or reproduce the published form of this manuscript, or allow others to do so, for the United States Government purposes. The Department of Energy will provide public access to these results of federally sponsored research in accordance with the DOE Public Access Plan (<http://energy.gov/downloads/doe-public-access-plan>).

## Author contributions

P.D. and T.A.M. developed the DCA++ code. L.F.L., Y.Z., A.M., and E.D. developed the bilayer two orbital model. T.A.M. designed the project, performed the calculations, analyzed the results, and wrote the manuscript with contributions from all the co-authors.

## Competing interests

The authors declare no competing interests.

## Additional information

**Supplementary information** The online version contains supplementary material available at <https://doi.org/10.1038/s41535-026-00849-9>.

**Correspondence** and requests for materials should be addressed to Thomas A. Maier.

**Reprints and permissions information** is available at <http://www.nature.com/reprints>

**Publisher's note** Springer Nature remains neutral with regard to jurisdictional claims in published maps and institutional affiliations.

**Open Access** This article is licensed under a Creative Commons Attribution 4.0 International License, which permits use, sharing, adaptation, distribution and reproduction in any medium or format, as long as you give appropriate credit to the original author(s) and the source, provide a link to the Creative Commons licence, and indicate if changes were made. The images or other third party material in this article are included in the article's Creative Commons licence, unless indicated otherwise in a credit line to the material. If material is not included in the article's Creative Commons licence and your intended use is not permitted by statutory regulation or exceeds the permitted use, you will need to obtain permission directly from the copyright holder. To view a copy of this licence, visit <http://creativecommons.org/licenses/by/4.0/>.

© UT-Battelle, LLC and Ling-Fang Lin, Yang Zhang, Adriana Moreo, Elbio Dagotto 2026